Applied Physics Express **12**, 011002 (2019)
https://doi.org/10.7567/1882-0786/aaee8d

LETTER

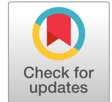

Synthesis and photoluminescence properties of hexagonal BGaN alloys and quantum wells

Qingwen Wang, Rakib Uddin, Xiaozhang Du, Jing Li, Jingyu Lin*, and Hongxing Jiang*

Department of Electrical and Computer Engineering, Texas Tech University, Lubbock, TX 79409, United States of America

*E-mail: hx.jiang@ttu.edu

Received October 8, 2018; accepted November 5, 2018; published online December 3, 2018

Hexagonal boron nitride (*h*-BN) has emerged as an important extreme bandgap semiconductor as well as a two-dimensional material. Achieving the ability for tuning the optoelectronic properties through alloying and heterojunction will further expand the applications of *h*-BN. By utilizing *h*-BN epilayer as a template, the synthesis of BN-rich $B_{1-x}Ga_xN$ alloys and quantum wells crystalized in the hexagonal phase has been demonstrated for the first time by metal organic chemical vapor deposition. The incorporation of Ga tends to enhance the conductivity. A blue shift in the band-edge emission upon the formation of *h*-BN/BGaN/BN QW has been observed, indicating the feasibility for heterojunction formation.
© 2018 The Japan Society of Applied Physics

Hexagonal boron nitride (*h*-BN) is the only layer-structured material among the traditional III-nitride wide bandgap semiconductor family members with excellent thermal, mechanical, and optical properties.[1–10] On the other hand, among the layer-structured or two-dimensional (2D) material system, *h*-BN possesses an exceptionally large energy bandgap of ~6.4 eV. The demonstrations of solid-state neutron detectors with a record high detection efficiency based on B-10 enriched *h*-BN epilayers with large thicknesses (~50 μm)[8,9] and *h*-BN/AlGaN p–n heterojunction formation[6,7] have already expanded the applications of III-nitride wide bandgap semiconductors in technologically significant areas of solid-state neutron detectors[8,9] and deep UV photonics.

As with all other compound semiconductors, achieving the ability for tuning the optoelectronic properties through alloying and heterojunction formation will further expand the applications of *h*-BN. One way to achieve a tunable energy bandgap in *h*-BN is to form alloys with GaN. However, the equilibrium phase of GaN is wurtzite, whereas that of BN is hexagonal. As such, crystallization of BGaN alloys in hexagonal lattice has not been attempted experimentally. Recent theoretical and experimental studies have shown that few layers of GaN and AlN could crystallize into 2D hexagonal layered structure in freestanding or substrate-supported states,[11,12] pointing to the possibility for synthesizing layer-structured *h*-BGaN alloys. With the recent advances in synthesizing *h*-BN epilayers by metal organic chemical vapor deposition (MOCVD),[6–10] we are now provided with an ideal template to explore the epitaxial growth of layered *h*-BGaN alloys. In this work, we report the first attempt of synthesizing via MOCVD and the photoluminescence (PL) emission and electrical properties of layered *h*-BGaN alloys and *h*-BN/BGaN/BN quantum wells (QWs).

A set of *h*-BGaN samples of about 10 nm in thickness were grown using triethylboron (TEB), ammonia (NH_3), and trimethylgallium (TMGa) as precursors for B, N, and Ga, respectively, and hydrogen as a carrier gas. The alloy composition was controlled via the variation of the TMGa flow rate (F_{Ga}) while keeping both the TEB and NH_3 flow rates constant. Prior to the deposition of *h*-BGaN, a 10 nm thick *h*-BN epilayer was first deposited on *c*-plane sapphire (Al_2O_3) substrate at ~1350 °C to serve as a template. The use of *h*-BN templates with a reasonable crystalline quality is necessary to support the crystallization of BGaN alloys into the intended hexagonal lattice. Figure 1 shows the X-ray diffraction (XRD) $\theta-2\theta$ scan for one of our *h*-BN epilayers of about 1 μm in thickness deposited on *c*-plane sapphire at a growth temperature of $T_g \sim 1350$ °C, which clearly reveals only the diffraction peaks for hexagonal phase BN and sapphire substrate. The position of 26.70° for the *h*-BN (0002) diffraction peak yields a *c*-lattice constant of ~6.67 Å, which is close to the bulk *c*-lattice constant of *h*-BN ($c = 6.66$ Å).[13,14] The linewidth of the XRD rocking curves of the *h*-BN (0002) peak for epilayers grown at relative high temperatures is nearly 380 arcsec.[6] In comparison with other III-nitride materials, the linewidth of XRD rocking curve of *h*-BN epilayers is still 5–8 times broader than those of high quality AlN epilayers deposited on *c*-plane sapphire substrates (~60 arcsec).[15] To accommodate the incorporation of Ga while retaining a reasonable crystalline quality, the growth temperature employed for *h*-BGaN alloy growth was 1225 °C (substrate temperature). Crystalline structure was characterized by XRD measurements. Atomic compositions of B, N, and Ga were determined using X-ray photoelectron spectroscopy (XPS). The PL measurement system used consists of a frequency quadrupled 100 fs Ti: sapphire laser as an excitation source with an excitation photon energy set around 6.28 eV. A 1.3 m monochromator

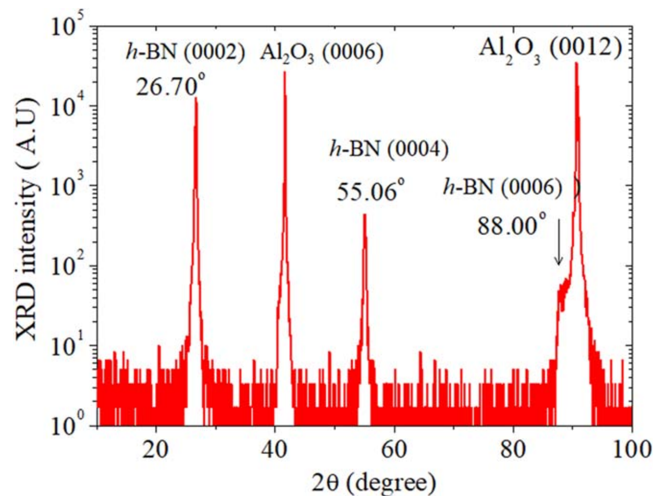

Fig. 1. (Color online) XRD $\theta-2\theta$ scan for an *h*-BN epilayer of about 1 μm in thickness deposited on *c*-plane sapphire at a growth temperature of $T_g \sim 1350$ °C.

© 2018 The Japan Society of Applied Physics

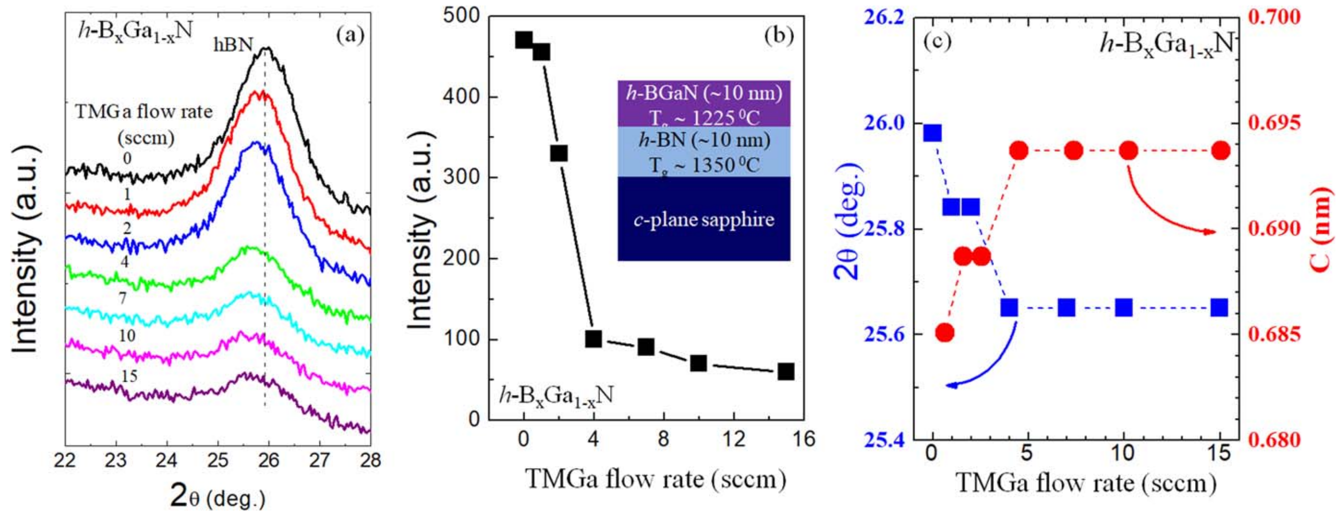

Fig. 2. (Color online) (a) XRD $\theta{-}2\theta$ scans of *h*-BGaN alloys grown under different TMGa flow rates at a growth temperature of $T_g \sim 1225$ °C. (b) The XRD (0002) diffraction peak intensity of *h*-BGaN as a function of the TMGa flow rate. The inset shows the layer structure of *h*-BGaN alloys used in this study. (c) The XRD (0002) diffraction peak position (left axis) and the corresponding *c*-lattice constant (right axis) vs. the TMGa flow rate.

in conjunction with a microchannel plate photomultiplier tube and a single photon counting detection system were used to disperse and record the PL signal.

XRD $\theta{-}2\theta$ scan results are shown in Fig. 2(a) for *h*-BGaN alloys grown under varying TMGa flow rate (F_{Ga}) from 0 to 15 standard cubic centimeters per minute (sccm). Although the crystalline quality of these thin layers grown at a lower temperature of 1225 °C is inferior in comparison to the *h*-BN epilayer deposited at a higher temperature of 1350 °C, all *h*-BGaN alloy samples exhibit diffraction peaks near 26°, which is close to that of the *h*-BN (0002) diffraction peak shown in Fig. 1. The results are therefore an indicative that these alloys have been crystallized into a nearly hexagonal lattice, although not a perfect one. We note that XRD $\theta{-}2\theta$ scans shown in Fig. 2(a) did not resolve the peaks for the underneath 10 nm *h*-BN, due most likely to these reasons: (1) The peak for *h*-BN is very close to those of *h*-BGaN, (2) the underneath *h*-BN layer is fairly thin, and (3) the property of the top *h*-BGaN layer is dominant. Figure 2(b) plots the (0002) XRD $\theta{-}2\theta$ peak intensity as a function of F_{Ga}, which exhibits an initial decrease followed by almost no change, with the onset point occurring at $F_{Ga} = 4$ sccm. Based on the measured $\theta{-}2\theta$ peak positions, we calculated the corresponding *c*-lattice constants of *h*-BGaN alloys and the results are summarized in Fig. 2(c), revealing that the *c*-lattice constant of *h*-BGaN increases initially and then saturates at about 6.94 Å with the onset point occurring at $F_{Ga} = 4$ sccm. Other than the alloying effects, as the theoretically calculated *a*-lattice constant of single layer *h*-GaN is $a = 3.21$ Å[12] and the *a*-lattice constant of *h*-BN is 2.5 Å,[13,14] *h*-BGaN epilayers grown on *h*-BN templates are expected to undergo a compressive strain. Therefore, an increase in the inter-plane distance ($c/2$) is expected with the incorporation of Ga. The observation of the onset point occurring at $F_{Ga} = 4$ sccm seems to suggest that only a limited amount of Ga atoms can be incorporated into *h*-BGaN. This may be related to the fact that the temperature employed for the growth of this set of *h*-BGaN alloys is higher than the decomposition temperature of GaN. However, due to the strong B–N bond, we have chosen a relatively high growth temperature of 1225 °C with the intention to promote the crystallization of BGaN alloys into the hexagonal phase. Furthermore, there may exist a miscibility gap in forming the *h*-BGaN alloys, similar to the scenarios in InGaN[16] and *h*-BCN[17,18] alloys in which the phase separation was caused by lattice mismatch and the bond energy difference among different atomic bonds, respectively. In *h*-BGaN, although the theoretical studies predicated that GaN could crystallize into hexagonal phase,[12] the difference in the equilibrium crystal structures between *h*-BN (hexagonal) and GaN (wurtzite) could limit the GaN fraction in *h*-BGaN at a given growth temperature. However, much more theoretical and experimental works are needed to understand the phase diagram of the *h*-BGaN alloy system.

Since XRD $\theta{-}2\theta$ scans provide information concerning the *c*-lattice constants and there are no available data for the *c*-lattice constant of *h*-GaN, we are unable to estimate the composition of Ga in *h*-BGaN alloys using Vegard's law. XPS were measured for three *h*-BGaN alloys grown under different TMGa flow rates. Samples were successively etched using low energy (500 V) Ar^+ ions and high-resolution tight scans were taken after each etching step. XPS spectra of a representative sample grown at $F_{Ga} = 15$ sccm are shown in Fig. 3(a) for B 1s, N 1s, and Ga 3d. No other transitions except B 1s, N 1s, and Ga 3d were detected from these samples. The average B, N, and Ga compositions in this sample are ~46.6%, 49.9%, and 3.5%, respectively, corresponding to *h*-$B_{1-x}Ga_xN$ alloy with $x = 0.07$. Based on the Ga compositions (x) in *h*-$B_{1-x}Ga_xN$ determined by XPS measurements, Fig. 3(b) plots the dependence of x in *h*-$B_{1-x}Ga_xN$ alloys on F_{Ga}, which reveals that x vs. F_{Ga} can be described by the following equation,

$$x = x_0[1 - \exp(-F_{Ga}/A)], \tag{1}$$

where x_0 denotes the saturation value of Ga composition and A describes an exponential dependence of x in *h*-$B_{1-x}Ga_xN$ with F_{Ga}. The least squares fit between the experimentally measured Ga compositions and Eq. (1) yielded $x_0 = (7.2 \pm 0.2)\%$ and $A = 2.14 \pm 0.17$ sccm. The Ga composition saturation behavior shown in Fig. 3(b) is consistent with the observed onset

© 2018 The Japan Society of Applied Physics

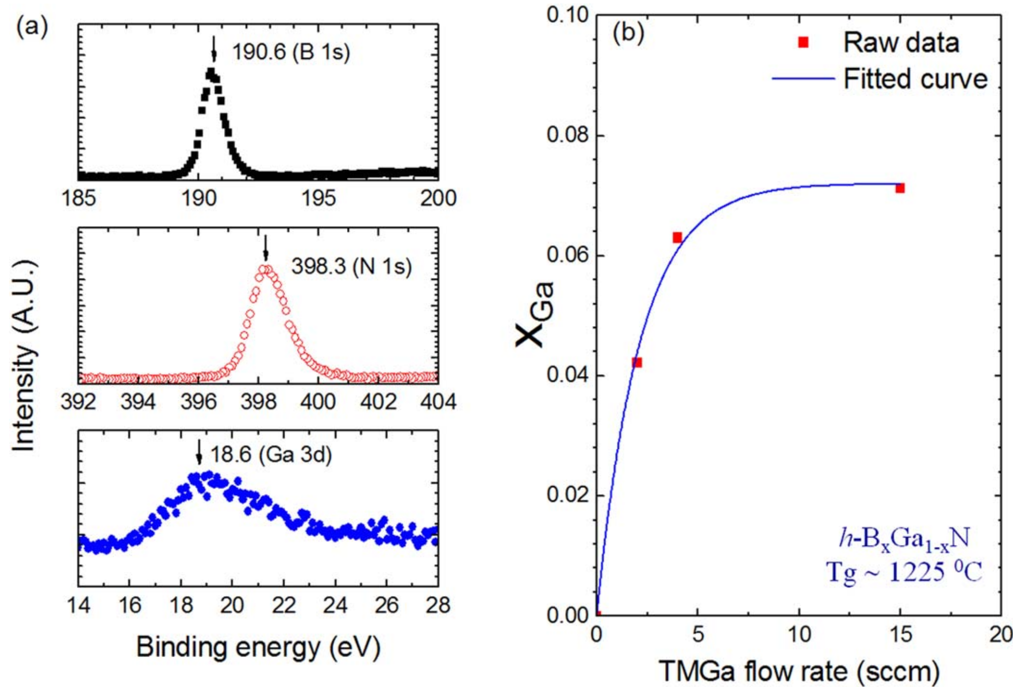

Fig. 3. (Color online) XPS spectra of an h-BGaN sample grown at TMGa flow rate = 15 sccm for B 1s, N 1s, and Ga 3d peaks. (b) The Ga composition (x) in h-$B_{1-x}Ga_xN$ alloys obtained via XPS measurements vs. the TMGa flow rate. The solid curve is the least squares fit of data with Eq. (1).

behavior exhibited in the dependence of the XRD intensity and c-lattice constant on the TMGa flow rate shown in Figs 2(b) and 2(c).

Since undoped h-BN is highly insulating and unintentionally doped GaN is usually conductive, one expects that the conductivity of h-$B_{1-x}Ga_xN$ alloys increases with an increase in x. Since these samples are BN-rich and hence electrically resistive, we utilized a metal–semiconductor–metal (MSM) device architecture consisting of micro-strip interdigital fingers to characterize their electrical resistivities. The photolithography technique was used to pattern the interdigital fingers. The MSM structure has a device size of $0.5\,\mathrm{mm} \times 0.5\,\mathrm{mm}$ with metal strips of $6\,\mu$m in width and spacing between the metal strips of $9\,\mu$m, as shown in Fig. 4(a). Metal contacts consisting of bi-layers of Ti/Al (20 nm/30 nm) were deposited by e-beam evaporation.[19] The dark I–V characteristics of two different h-$B_{1-x}Ga_xN$ alloy samples together with a 10 nm thick h-BN template are shown in Fig. 4(b). From the dimensions of the interdigital fingers shown in Fig. 4(a), the deduced electrical resistivities for h-BGaN were $\rho \approx 5 \times 10^{10}$, 5×10^6, and $2 \times 10^6\,\Omega\,\mathrm{cm}$ for $x = 0$, 0.045, and 0.07, respectively, corresponding to an enhancement in the electrical conductivity of more than 4 orders of magnitude as the Ga composition in h-$B_{1-x}Ga_xN$ was increased from 0 to 0.07. This ability of conductivity control is expected to be very useful for device applications.

With the baseline for the growth of h-BGaN epilayers established, the growth of an h-BN/$B_{1-x}Ga_xN$/BN QW was attempted. As for the growth of h-BGaN epilayers, prior to the deposition of a 2 nm thick h-BGaN QW, a 10 nm thick h-BN epilayer was first deposited on sapphire substrate at 1350 °C to serve as a template as well as the bottom barrier layer. In order to minimize the effect of decomposition of GaN in the well region, the growth temperature of the QW and the top h-BN barrier was set to be the same as that of the h-BGaN epilayers. The targeted GaN fraction in the well

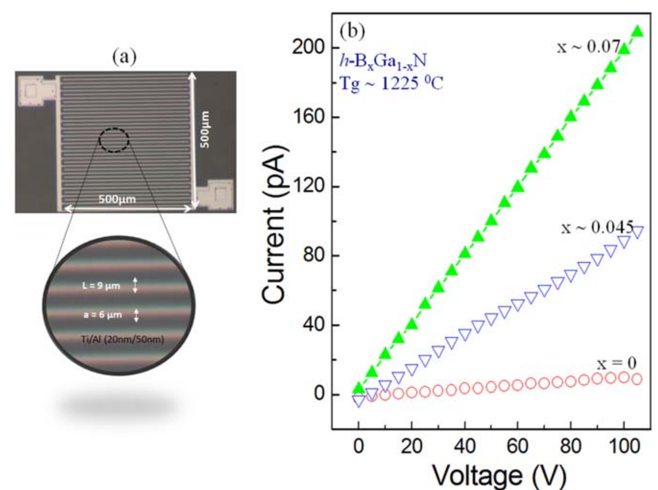

Fig. 4. (Color online) (a) Micrograph of a representative h-$B_{1-x}Ga_xN$ MSM device for I–V characterization. The device has a size of $0.5\,\mathrm{mm} \times 0.5\,\mathrm{mm}$ with metal strips of $6\,\mu$m in width and spacing between the metal strips of $9\,\mu$m. (b) Dark I–V characteristics of two different h-$B_{1-x}Ga_xN$ samples, $x = 0.045$ and 0.07. Dark I–V characteristic of a 10 nm thick h-BN template is also included for comparison.

region was ~4%. For comparison, a 2 nm thick h-BGaN epilayer without the top h-BN barrier was also grown at the identical conditions as those of the h-BGaN well region in the BN/$B_{1-x}Ga_xN$/BN QW. Figure 5 presents 10 K PL spectra of two samples (a) h-BN/BGaN/BN QW and (b) h-BGaN alloy, along with schematics of the layer structures. The impurity related emission peaks around 4 eV are dominant, which have been observed previously in h-BN and attributed to a donor–acceptor pair recombination line and its phonon replicas involving the 200 meV longitudinal optical phonon mode.[20–22] By adopting the understanding from h-BN,[5,20–22] the band-edge emission line near 5.55 eV in h-BGaN alloy can be attributed to the recombination of bound excitons (or self-trapped

© 2018 The Japan Society of Applied Physics

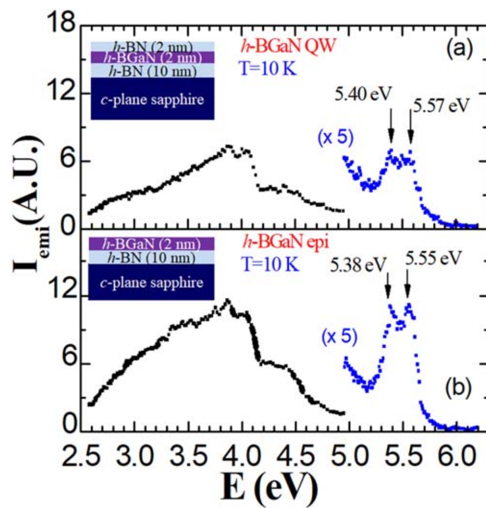

Fig. 5. (Color online) Low temperature (10 K) PL spectra for (a) h-BN/$B_{1-x}Ga_xN$/BN QW ($x \sim 0.04$) and (b) h-$B_{1-x}Ga_xN$ ($x \sim 0.04$) epilayer. The layer structures are shown as insets.

excitons).[23–25] Another emission line at 5.38 eV which is 170 meV lower than the main emission line at 5.55 eV is very pronounced in both samples. This observed energy separation is the same as the phonon energy of E_{2g} symmetry vibration mode in h-BN ($\Delta\sigma - 1371\ cm^{-1}$),[26] which suggests that the 5.38 eV emission line is most likely the 1-phonon replica of the 5.55 eV zero-phonon line. Since the E_{2g} symmetry vibration mode corresponds to the in-plane stretch of B and N atoms, the observation of a pronounced phonon replica line involving E_{2g} symmetry vibration mode seems to corroborate the fact that h-BGaN alloy has a reasonable layered structure.

In comparison, the PL spectral line shapes of the 2 nm thick h-BGaN epilayer and 2 nm h-BGaN QW are quite similar. However, a careful inspection reveals that both the band-edge emission and its phonon replica lines in h-BGaN QW were slightly blue shifted by ~20 meV with respect to those in h-BGaN epilayer. This seems to suggest that we have successfully synthesized a layer-structured QW and that the formation of h-BN/BGaN/BN QW induces a quantum confinement effect, as in the conventional QWs. However, due to the larger exciton binding energy (~0.7 eV)[2,3,19,27] and smaller exciton Bohr radius (~0.1 nm)[27] in h-BN (and hence in B-rich h-BGaN), we expect the confinement effect in h-BGaN QW to be less visible than that in more conventional QWs (e.g., GaN/AlN) with the same well width.

In summary, by utilizing h-BN epilayer as a template, we have successfully synthesized for the first time BN-rich layer-structured h-$B_{1-x}Ga_xN$ alloys and QWs via MOCVD with a maximum Ga composition up to about 7%. The formation of h-BGaN alloy enables the ability for electrical conductivity control as well as the formation of layer-structured QWs and heterostructures. These layer-structured alloys and QWs represent a new material system for the exploration of novel physical properties as well as deep UV photonic devices. However, many issues such as Ga composition saturation, possible phase separation, critical thickness, and growth processes for further improving the overall material quality still need to be addressed.

Acknowledgment This work is supported by ARO (W911NF-16-1-0268) and monitored by Dr. Michael Gerhold. The structural characterization efforts were partially supported by NSF (ECCS-1402886). HJ and JL are grateful to the AT&T Foundation for the support of Ed Whitacre and Linda Whitacre endowed chairs.

ORCID iDs Jingyu Lin https://orcid.org/0000-0003-1705-2635

1) N. G. Chopra, R. J. Luyken, K. Cherrey, V. H. Crespi, M. L. Cohen, S. G. Louie, and A. Zettl, Science **269**, 966 (1995).
2) K. B. Arnaud, S. Lebe'gue, P. Rabiller, and M. Alouani, Phys. Rev. Lett. **96**, 026402 (2006).
3) L. Wirtz, A. Marini, and A. Rubio, Phys. Rev. Lett. **96**, 126104 (2006).
4) Y. Kubota, K. Watanabe, O. Tsuda, and T. Taniguchi, Science. **317**, 932 (2007).
5) K. Watanabe, T. Taniguchi, and H. Kanda, Nat. Mater. **3**, 404 (2004).
6) S. Majety, J. Li, X. K. Cao, R. Dahal, B. N. Pantha, J. Y. Lin, and H. X. Jiang, Appl. Phys. Lett. **100**, 061121 (2012).
7) H. X. Jiang and J. Y. Lin, Semicond. Sci. Technol. **29**, 084003 (2014).
8) A. Maity, S. J. Grenadier, J. Li, J. Y. Lin, and H. X. Jiang, Appl. Phys. Lett. **111**, 033507 (2017).
9) A. Maity, S. J. Grenadier, J. Li, J. Y. Lin, and H. X. Jiang, J. Appl. Phys. **123**, 044501 (2018).
10) X. Yang, S. Nitta, K. Nagamatsu, S. Y. Bae, H. J. Lee, Y. Liu, M. Pristovsek, Y. Honda, and H. Amano, J. Cryst. Growth **482**, 1 (2018).
11) D. X. Wu, M. G. Lagally, and F. Liu, Phys. Rev. Lett. **107**, 236101 (2011).
12) D. Kecik, A. Onen, M. Konuk, E. Gürbüz, F. Ersan, S. Cahangirov, E. Aktürk, E. Durgun, and S. Ciraci, Appl. Phys. Rev. **5**, 011105 (2018).
13) R. W. Lynch and H. G. Drickamer, J. Chem. Phys. **44**, 181 (1966).
14) R. S. Pease, Acta Crystallogr. **5**, 356 (1952).
15) B. N. Pantha, R. Dahal, M. L. Nakarmi, N. Nepal, J. Li, J. Y. Lin, H. X. Jiang, Q. S. Paduano, and D. Weyburne, Appl. Phys. Lett. **90**, 241101 (2007).
16) I. Ho and G. B. Stringfellow, Appl. Phys. Lett. **69**, 2701 (1996).
17) K. Yuge, Phys. Rev. B **79**, 144109 (2009).
18) M. R. Uddin, J. Li, J. Y. Lin, and H. X. Jiang, J. Appl. Phys. **117**, 215703 (2015).
19) T. C. Doan, J. Li, J. Y. Lin, and H. X. Jiang, Appl. Phys. Lett. **109**, 122101 (2016).
20) L. Museur and A. Kanaev, J. Appl. Phys. **103**, 103520 (2008).
21) M. G. Silly, P. Jaffrennou, J. Barjon, J.-S. Lauret, F. Ducastelle, A. Loiseau, E. Obraztsova, B. Attal-Tretout, and E. Rosencher, Phys. Rev. B **75**, 085205 (2007).
22) X. Z. Du, J. Li, J. Y. Lin, and H. X. Jiang, Appl. Phys. Lett. **106**, 021110 (2015).
23) K. Watanabe and T. Tanniguchi, Phys. Rev. B **79**, 193104 (2009).
24) L. Museur et al., Phys. Status Solidi RRL **5**, 214 (2011).
25) S. Majety, X. K. Cao, J. Li, R. Dahal, J. Y. Lin, and H. X. Jiang, Appl. Phys. Lett. **101**, 051110 (2012).
26) R. J. Nemanich, S. A. Solin, and R. M. Martin, Phys. Rev. B **23**, 6348 (1981).
27) X. K. Cao, B. Clubine, J. H. Edgar, J. Y. Lin, and H. X. Jiang, Appl. Phys. Lett. **103**, 191106 (2013).

© 2018 The Japan Society of Applied Physics